

# Wake energy analysis method applied to the Boxprop propeller concept

**Alexandre Capitaó Patrao, first author, corresponding author**

Chalmers University of Technology  
Department of Applied Mechanics  
Gothenburg, SE-41296  
Sweden  
alexandre.capitao.patrao@gmail.com

**Tomas Grönstedt, second author**

Chalmers University of Technology  
Department of Applied Mechanics  
Gothenburg, SE-41296  
Sweden  
tomas.gronstedt@chalmers.se

**Richard Avellán, third author**

GKN Aerospace Sweden  
Trollhättan, SE-46181  
Sweden  
richard.avellan@gknaerospace.com

**Anders Lundbladh, fourth author**

GKN Aerospace Sweden & Chalmers University of Technology  
Trollhättan, SE-46181  
Sweden  
anders.lundbladh@gknaerospace.com

**Keywords: Aircraft propeller, Wake energy analysis, Computational Fluid Dynamics, Open Rotor**

**Declaration of interest: None.**

## **ABSTRACT**

*Inspired by Prandtl's theory on aircraft wings with minimum induced drag, the authors have introduced a double-bladed propeller, the Boxprop, intended for high-speed flight. The basic idea is to join*

*the propeller blades pairwise at the tip to decrease tip vortex strength and improve mechanical properties compared to a conventional propeller.*

*The present work develops a wake analysis method allowing an energy breakdown of the flow as well as making the irreversibility of the flow explicit. The method quantifies the strength of flow features such as tip vortices and wakes in terms of engine power. In contrast to existing work, this method removes assumptions of uniform flow, radial flow, and constant static pressure in the propeller jet.*

*The results of the wake analysis method can be summarized into three key findings 1) the energy in the tip-vortex of the Boxprop design is comparatively speaking non-existent 2) the swirl energy level of the Boxprop is higher and this turbomachine is thus more in need of a downstream counter-rotating blade to recover the energy 3) the Boxprop develops a much larger part of its thrust closer to the hub. Analysis of this aspect of the flow reveals that blade interference approaching the tip, where the blades in a pair are more closely spaced, is quite pronounced. In turn, this indicates that maximum efficiency Boxprop designs are more likely to be obtained by having larger axial separation of the two blades.*

## **1 INTRODUCTION**

Increased competition, environmental awareness, and energy security are some of the drivers behind the development of new state-of-the-art technologies for aero engines. The introduction of the open rotor engine could cause significant fuel savings, mainly due to its increased bypass ratio and lower nacelle drag. Already in the 1970s, as a consequence of the OPEC oil embargo, NASA initiated several R&T programs that were aiming for substantial reductions in fuel consumption of the US civil- and military aircraft [1]. The perhaps most promising and challenging concept at the time was the counter-rotating open rotor concept. Intensive research and development during the 1970s and 1980s ended with a series of successful flight demonstrations that proved the

concept to be as promising as expected, although there were some remaining issues, for instance regarding the noise levels [2].

In the beginning of the 21st century the oil price, corrected for inflation, reached about the same levels as that of the mid 1970s and the search for energy efficient engine technologies intensified yet again. The open rotor engine concept is once more being developed; this time led by Europe within the EC FP7 research program Clean Sky [3], and ground tests of a full scale open rotor demonstrator have started as of 2017 [4].

Inspired by Prandtl's theory on aircraft wings with minimum induced drag [5], the authors in 2009 conceived the concept of a double-bladed propeller intended for high-speed flight [6, 7]. The inspiration stems from the box wing for aircraft (see Fig. 1 [8]), which could reduce the induced drag in aircraft wings by approximately 30% [9]. Aircraft concept designs incorporating box wings have been suggested both by Lockheed Martin and NASA [10]. For propellers, the basic idea is to join the blades pair-wise at the tip (see Fig. 4) to improve aerodynamics and mechanical properties compared to conventional propeller blades [11].

The main hypotheses for this propeller concept, hereinafter called the Boxprop, are increased propeller efficiency and reduced interaction noise due to tip-vortex suppression and an increased structural integrity due to the connected blade-pairs. The expected increased rigidity might allow forward-sweep of the propeller blade, which for a counter-rotating setup would increase the intra-rotor axial distance and thereby the mixing of blade wakes and tip vortices. Weakening these flow structures could

potentially decrease interaction noise, so it would be of great benefit to be able to compare the strength of the wakes and tip vortices for different blade designs. The operational region of an open rotor is large, from low speed (ground roll and take-off) to climb and cruise up to high subsonic Mach numbers, and further to reverse thrust generation, necessitating the use of pitch control. Pitch control is achieved by placing the blade roots on a common base, which can then rotate the entire Boxprop to match the flow. A description and an illustration of the pitch control mechanism can be found in a previous article by the authors [12].

This paper presents a propeller energy wake analysis method which enables a systematic breakdown of the various losses in the flow around a propeller and provides the ability to distinguish and quantify the strength of tip vortices and wakes. Quantifying these flow features in terms of shaft power allows different propellers to be compared by the amount of shaft power being spent on generating swirl, radial flow, tip vortex flow, and flow irreversibilities. The method also removes some of the assumptions inherent to existing methods, more specifically it removes the assumptions of uniform flow, no radial flow, and constant static pressure found in [13]. The ability to distinguish the tip vortices and wakes also sets this new method apart from similar published work for the energy analysis of aircraft [14] and propellers [13]. The method derived herein will be used for showing a number of systematic differences between a conventional propeller and a Boxprop. The most striking difference between the two will be a significantly lower tip vortex kinetic energy of the Boxprop relative to the conventional propeller design. The developed method will also reveal that the Boxprop design

features more swirl kinetic energy than its conventional counterpart due to the interference between the blades in each blade pair. It will therefore be argued that the Boxprop is more in need of a downstream counter-rotating blade to recover the swirl energy. The analysis method will also be used to suggest systematic geometry alterations in the current Boxprop design practice, with the intent to reduce the more pronounced blade interference observed for the Boxprop.

## 2 WAKE ANALYSIS METHOD DERIVATION

In this section an energy analysis method for a propeller wake is derived, extended and applied to two propeller variants. This wake analysis method relates the energy changes in particles that travel through a rotor to the work added to the flow and enables a systematic breakdown of the added work into entropy lost work, reversible pressure changes, and kinetic and turbulent energy changes. In other words, it allows the estimation of terms that are propulsively beneficial, recoverable, or pure losses in the flow. Additionally, the method will utilize a decomposition of the flowfield which very clearly distinguishes the tip vortices and wakes from the mean flow.

Consider an elemental fluid particle flowing through a turbomachine (Fig. 2). In a coordinate system rotating with the rotor, the flow will be steady. However, the velocities will be defined in reference to a stationary frame. The work per unit time added to the particle between a point upstream of the rotor and a control point downstream of the rotor lying on a plane,  $d\dot{W}$ , can be calculated from the total enthalpy change  $\Delta h_0$ , as specified in Eq. (1).

$$d\dot{W} = \Delta h_0 d\dot{m} = \Delta h_0 \rho_2 u_n dA \quad (1)$$

$$u_n = u_x \quad (2)$$

Henceforth it is assumed that the wake is evaluated in planes normal to the axial direction. Thus, the normal velocity  $u_n$  becomes the axial velocity, as is manifested by Eq. (2).

In order to account for all the power transferred from the propeller ( $P_{shaft}$ ) to the working fluid, the particle work per unit time is integrated over an annular area  $A$  behind the propeller:

$$P_{shaft} = \int_A d\dot{W} = \int_A \Delta h_0 \rho_2 u_n dA \quad (3)$$

The slice of area  $A$  corresponding to one propeller blade passage is shown in Fig.

2. The change in total enthalpy is calculated as the difference between the points on the plane behind the propeller and far upstream, per Eq. (4).

$$\Delta h_0 = h_{0,2} - h_{0,1} \quad (4)$$

The total enthalpy change can be expanded into its constituents:

$$\Delta h_0 = \Delta h + \Delta \left( \frac{1}{2} u_i u_i \right) + \Delta k \quad (5)$$

The enthalpy term can be further decomposed into an irreversible entropy lost work term  $\phi_s$  and a reversible pressure work term  $\phi_p$  by using the Gibbs relation. For a particle travelling along a streamline, it reads:

$$dh = Tds + vdp \quad (6)$$

$$\rightarrow h_2 - h_1 = \underbrace{\int_1^2 T ds}_{\phi_s} + \underbrace{\int_1^2 v dp}_{\phi_p} \quad (7)$$

This expression is exact, but cumbersome to evaluate numerically in an accurate and conservative manner. Conservation of energy has traditionally been an issue when integrating along streamlines which pass through shocks or strong gradients, which resulted in different values in the LHS and RHS of Eq. (7). Additionally, it requires the CFD software to construct a very large amount of streamlines originating from the integration plane and extending them upstream to the inlet. An alternative approach, which is used both by Hall [13], Denton [15], Dixon [16], and Miller [17], employs the following approximate expression for the entropy lost work term:

$$\phi_s = \int_1^2 T ds \approx T_\infty (s_2 - s_1) \quad (8)$$

This approach has been compared to the exact formulation in Eq. (7) for an entire blade passage, and the resulting difference in entropy lost work only accounted to 0.1% of the propeller shaft power ( $P_{shaft}$ ). Similar conclusions have previously been reached by Denton [15], and the expression is also very similar to the expression for irreversibility used in the exergy framework [18]. An increase in the entropy lost work  $\phi_s$  will be due to the losses in the blade boundary layer (viscous and turbulent dissipation), shocks, and mixing (heat addition is not included in the scope of this paper). The pressure term  $\phi_p$  in Eq. (7) is then calculated using Eq. (9) below:

$$\phi_p = \int_1^2 v dp \approx (h_2 - h_1) - T_\infty (s_2 - s_1) \quad (9)$$

An increasing pressure work term  $\phi_p$  can be due to an increase in pressure through the propeller plane, as is described by simpler propeller theories such as the *Actuator Disc Theory*. A decrease in the pressure work can be found downstream of the propeller disc, where it is converted into axial kinetic energy.

The turbulent kinetic energy increase  $\Delta k$  in Eq. (5) occurs mainly in the boundary and shear layers present in the flow, which for a propeller corresponds to the wetted surfaces, wakes, and tip vortices. Far enough downstream, this term is converted into the entropy lost work  $\phi_s$  through turbulent dissipation.

The kinetic energy term in Eq. (5) can be further expanded into its components, in their cylindrical coordinates:

$$\frac{1}{2}u_i u_i = \frac{1}{2}(u_x^2 + u_r^2 + u_\theta^2) \quad (10)$$

Equations (3) to (10) will yield the composition of the shaft power in terms of the flow variables in the wake. Assuming that the flow is purely axial and uniform far upstream results in the following expression:

$$P_{shaft} = \int_A \rho_2 u_n \left[ \phi_s + \phi_p + \frac{1}{2} \left( (u_{x,2}^2 - u_{x,1}^2) + u_{r,2}^2 + u_{\theta,2}^2 \right) + (k_2 - k_1) \right] dA \quad (11)$$

The term representing the increase in axial kinetic energy can be rewritten as shown below:

$$\frac{1}{2}(u_{x,2}^2 - u_{x,1}^2) = u_{x,1} \Delta u_x + \frac{1}{2}(\Delta u_x)^2 \quad (12)$$

$$\Delta u_x = u_{x,2} - u_{x,1} \quad (13)$$

In Eq. (12), the second term is associated with the excess axial kinetic energy found in the jet downstream of the rotor, which can be considered a loss. The first term in Eq. (12) represents the increase in axial momentum of the jet due to the production of thrust by the rotor. For the case of a fully expanded jet at atmospheric conditions this term fully accounts for the produced thrust and the propulsive power. This term can, together with the pressure term  $\phi_p$ , be regarded as the propulsive power, since it accounts for the pressure increase close to the propeller disc, which would otherwise be neglected by only including the change in axial momentum. Incorporating the abovementioned terms into Eq. (11) yields:

$$P_{shaft} = \int_A \rho_2 u_n \left[ \phi_s + \phi_p + u_{x,1} \Delta u_x + \frac{1}{2} ((\Delta u_x)^2 + u_{r,2}^2 + u_{\theta,2}^2) + (k_2 - k_1) \right] dA \quad (14)$$

In order to capture the structure of the wake and tip vortex, the velocity components  $u_i(r, \theta)$  can be decomposed into a *circumferentially averaged velocity*  $U_i(r)$  and an associated *perturbation*  $v_i(r, \theta)$ :

$$u_i(r, \theta) = U_i(r) + v_i(r, \theta) \quad (15)$$

$$U_i = \frac{1}{\kappa} \int_0^{2\pi} \rho_2 u_n u_i d\theta \quad \kappa = \int_0^{2\pi} \rho_2 u_n d\theta \quad (16)$$

Assuming that the flow is purely axial and uniform far upstream and applying Eq. (15) to the kinetic energy terms of Eq. (14), one obtains:

$$(\Delta u_x)^2 = (\Delta U_x)^2 + (\Delta v_x)^2 \quad (17)$$

$$u_{r,2}^2 = U_{r,2}^2 + v_{r,2}^2 \quad (18)$$

$$u_{\theta,2}^2 = U_{\theta,2}^2 + v_{\theta,2}^2 \quad (19)$$

The cross-terms (e.g.  $2U_{r,2}v_{r,2}$ ) that would appear in Eq. (17) to (19) become zero when integrated in Eq. (14) and are therefore neglected. The perturbation terms ( $\Delta v_x$ ,  $v_{r,2}$  and  $v_{\theta,2}$ ) constitute the variation in velocity behind each blade of the propeller and do not carry any mean axial momentum, and therefore do not contribute to thrust. For a highly loaded propeller most of the energy in these terms are associated with the tip vortices and wakes of the blades. Initial results from the analysis of the structure of a propeller wake using the velocity decomposition in Eq. (15) and (16) were presented in [12]. The final expression for the wake analysis method is shown in Eq. (20), where terms marked in green contribute to propulsion, blue terms could be recoverable in a rear counter-rotating propeller, and the red terms denote losses.

$$P_{shaft} = \int_A \rho_2 u_n \left[ \phi_s + \phi_p + u_{x,1} \Delta u_x + \frac{1}{2} ((\Delta U_x)^2 + U_{r,2}^2 + U_{\theta,2}^2) + \frac{1}{2} ((\Delta v_x)^2 + v_{r,2}^2 + v_{\theta,2}^2) + (k_2 - k_1) \right] dA \quad (20)$$

The derived *wake analysis method* can be used to:

- Quantify the thermodynamic losses in terms of shaft power. This type of analysis could potentially also be applied on other types of turbomachinery such as axial compressors and turbines. The method is suitable for the comparison of different turbomachine variants (in this case propeller types).

- Recoverable energy terms, such as the swirl kinetic energy, can be calculated downstream of rotors, and the efficacy of downstream stators or counter-rotating rotors in eliminating swirl can be determined by applying the wake analysis method behind each rotor/stator.
- The strength of non-uniformities such as tip vortices and wakes can be quantified in terms of shaft power, which provides means for comparison of different designs.

Similar methods have been presented in the past which include some of these features, but with without the ability to quantify the strength of flow non-uniformities and additionally using simplifying assumptions.

### 3 PROPELLER PERFORMANCE PARAMETERS

Propeller performance is commonly specified in terms of the non-dimensional advance ratio, power coefficient, thrust coefficient, and propeller efficiency, as defined in Eq. (21) to (24).

$$J = \frac{V_{\infty}}{nD} \quad (21)$$

$$C_P = \frac{P_{shaft}}{\rho_1 n^3 D^5} \quad (22)$$

$$C_T = \frac{F_x}{\rho_1 n^2 D^4} \quad (23)$$

$$\eta_{prop} = \frac{F_x V_{\infty}}{P_{shaft}} \quad (24)$$

The *activity factor (AF)* is a related to the amount of power that the propeller can absorb:

$$AF = \frac{10^5}{D^5} \int_{R_{hub}}^{R_{tip}} cr^3 dr \quad (25)$$

## 4 PROPELLERS AND OPERATING POINT

To limit the computational cost while reaching above the transitional Reynolds number range, the diameters of the propellers were set to 0.75 m. Two propeller types are used, a conventional one (GPS609) inspired by the NASA SR-7L propeller from the Large-Scale Advanced Prop-Fan (LAP) [19] research program, and the Boxprop (GPX701). The two propellers in this paper have roughly the same thrust coefficients (see Table 2) and can be seen in Fig. 3 and Fig. 4. Design parameters for both propellers are displayed in Table 1. The propeller operating point is at Mach 0.75 and an altitude of 10 668 m under ISA [20] conditions, typical for cruise of a future passenger aircraft equipped with open rotor engines.

### 4.1 The conventional propeller

The eight-bladed conventional swept propeller (Fig. 3) named GPS609 was designed as a reference for the Boxprop. The design is based on the SR-7L, using the same number of blades, airfoil profile family (NACA16), propeller activity factor, thickness, and camber distributions. The sweep is similar, but the hub-to-tip-ratio is increased to 0.4 and the hub is cylindrical. The chords are scaled to match the SR-7L activity factor.

The blade geometry was generated using an in-house Blade Element/Vortex propeller design code based on the design methodology presented by Drela [21]. The obtained designs were then simulated with CFD in order to obtain more realistic performance estimates and to allow a close matching of the thrust to that of the GPX701.

#### **4.2 The Boxprop**

The five bladed Boxprop named GPX701 consists of pair-wise joined, forward swept blades. Each blade arch consists of a leading blade (LB) and a trailing blade (TB), see Fig. 4. The naming is based on which blade is leading when considering only the rotational velocity.

The use of five blades is an initial choice for the investigation of the concept, with an intent to get a similar performance as the SR-7L. In order to compare two propellers with unequal number of blades the propeller activity factor of the GPX701 is identical to the GPS609.

The NACA16 airfoil sections of the GPX701 are placed along an arch-shaped stacking line, with pre-specified chord, thickness, and camber distributions. These distributions are adjusted in order to limit the size of regions of supersonic flow in the blade passage.

The pitch was initially set as identical on both blade halves, which in some instances resulted in negative incidence on the inner part of the leading blade, lower thrust and decreased propeller efficiency. Consequently the GPX701 leading blade

angle-of-attack was increased to match the sectional thrust of the trailing blade

$a_{tr}/R_{tip} = 0.55$ , see Fig. 12.

## 5 SIMULATION METHODOLOGY

### 5.1 Computational domain

The computational domain is divided into a 2D, *outer stationary domain* and an *inner rotating domain*, the latter representing a sector with one blade (one blade pair for the Boxprop), as seen in Fig. 5. The large size of the inner domain was found necessary to accurately simulate the development of the blade tip vortex and wake. The domain opening is located 10 blade heights above the blade hub, and the domain extends axially 14 blade heights upstream and downstream of the blade. To accurately calculate performance (thrust and torque), a considerably smaller domain would suffice.

The multiblock hexahedral meshes were built using ICEM-CFD and the blocking structure arranged such that the mesh follows the helix shape of the wake structures at each radius and the tip vortex. The helix shape cannot continue indefinitely downstream of the propeller since the domain shape will start to become increasingly degenerated, leading to low mesh quality. Therefore, at a certain position downstream of the propeller, the domain becomes aligned with the axial direction.

For the *conventional blade*, the mesh blocking was done by assuming that the wake would generally follow the blade angle at each radius. The mesh region near the blade section can be seen in Fig. 6, where the wake block is visible to the right of the

airfoil. The Boxprop blocking structure is similar, with wake blocks extending downstream of the propeller, with the main difference being that the angle used for those two blocks is the same and taken as the average of the respective blade angles at each radius. The mesh sizing normal to blade surfaces was chosen in order to accommodate a low-Reynolds near wall formulation, resulting in  $y_{ave}^+ = 1.53$ , below the required  $y^+ < 2$  [22].

Modelling of the nacelle boundary layer was omitted for both propellers since it would add additional complexity to the analysis by increasing the number of parameters in the design space. Furthermore, the hub boundary layer is much smaller than the blade height, and the effect is then expected to be at most moderate for the design aspects studied in this paper.

A mesh study was performed in order to ensure convergence of the performance values and the wake analysis results. The wake blocks and surrounding blocks were refined mostly in the radial and tangential directions, which are the directions with the highest flow gradients. The mesh study ranged mesh sizes from 5 to 46 million cells. The study yielded propeller thrust, torque, and efficiency differences of less than 0.3%. The maximum absolute difference for the integrals of the individual terms in Eq. (20) are no larger than 0.25% of the shaft power. The final mesh sizes for the GPS609 and GPX701 simulations were 25 and 46 million cells, respectively. The difference is mainly due to the larger sector angle of the GPX701.

## 5.2 Numerical method

The CFD software used was ANSYS CFX, an implicit, finite volume based solver. The governing equations constitute the standard RANS equations, which are Favre-averaged due to the flow being compressible. The working fluid is treated as a thermally perfect gas, and the chosen turbulence model is the  $k - \omega$  SST model coupled with a low-Reynolds near wall formulation.

Convergence is measured via average residuals of the governing equations, global conservation, and measured performance parameters (e.g. thrust and power coefficients). A simulation is deemed converged when the residuals and global conservation parameters are in the order of  $10^{-5}$  and stable.

### 5.3 Boundary conditions

The *inlet* boundary conditions (see Fig. 5) are set through total temperature, total pressure and turbulence intensity, and the *outlet* boundary through a static pressure boundary condition. The *opening* surface uses an opening (entrainment) and zero gradient turbulence boundary condition [23].

*Rotational periodicity* is used both in the inner and outer domains, and the connection between the two domains is set through *frozen rotor interfaces*. These interfaces were used due to their frame-change capability and robustness [24]. The hub surfaces were all set as *free slip walls* while the propeller was set as a *no-slip wall*.

### 5.4 Wake analysis method implementation

Implementing the expressions in section 2 is done by relating the energy values at a plane *behind the propeller* (see Fig. 5) to the *upstream conditions*, which are evaluated at the inlet of the computational domain. The shaft power is obtained by calculating the torque acting on the propeller and multiplying with the rotational velocity, which is then used when normalizing Eq. (20). Evaluating the integrals of Eq. (20) for a number of planes downstream of the propeller and normalizing with propeller power yields axial trends for the energy distribution. These trends can be evaluated at an appropriate distance from the propeller to indicate how large the various loss terms are. The kinetic energy breakdown in Eq. (20) was computed using a post-processing routine developed in MATLAB.

## 6 RESULTS

### 6.1 Wake analysis

The loss terms of Eq. (14), repeated below for convenience, are presented for the GPS609 and for the GPX701 in Fig. 7.

$$P_{shaft} = \int_A \rho_2 u_n \left[ \phi_s + \phi_p + u_{x,1} \Delta u_x + \frac{1}{2} ((\Delta u_x)^2 + u_{r,2}^2 + u_{\theta,2}^2) + (k_2 - k_1) \right] dA$$

The loss terms are composed of the entropy loss  $\phi_s$ , the excess axial kinetic energy  $\frac{1}{2} \Delta u_x^2$ , and the radial kinetic energy  $\frac{1}{2} u_{r,2}^2$  of the jet. The swirl kinetic energy  $\frac{1}{2} u_{\theta,2}^2$  is also shown since it is a loss for a single propeller but could to a large extent be recovered in a downstream, counter-rotating propeller. The turbulent kinetic energy term was omitted

in Fig. 7 as it contributes by less than 0.5% to the total power flow. The loss terms are plotted on planes at a distance of  $0.2D$  downstream of the propeller trailing edge at  $r/R_{tip} = 0.75$ . This is a representative value for the position of a possible rear counter-rotating rotor in a CROR setup according to Negulescu [25].

Both the GPS609 and the GPX701 exhibit similar entropy loss values in the propeller wakes, but the peak entropy lost work value is found in the tip vortex region of the conventional propeller, a feature which is not present in the GPX701. Entropy lost work due to the passage shock of the GPX701 is faintly visible at the midspan position of the leading blade suction side. The location of the tip vortex is clearly visible in all four subplots for the GPS609, and in particular in the radial kinetic power flux plot. The radial component of the GPX701 in Fig. 7 does not show a circular tip vortex at this distance downstream of the propeller. The swirl power flux plots in Fig. 7 also showcase a higher amount of swirl for the GPX701 relative to the GPS609, and in particular an area of extensive swirl near the hub of the GPX701.

As was shown in section 2, the velocity components can be decomposed into a circumferential average and perturbation,  $u_i(r, \theta) = U_i(r) + v_i(r, \theta)$ , thereby capturing the kinetic energy bounded to the non-uniformities in the flow behind the blade. Fig. 8 shows the sum of the *perturbation* kinetic power fluxes and its components for the GPS609 and GPX701. The peak of the perturbation kinetic power fluxes are found in the tip vortex region of the GPS609, which is visible both in the sum of the perturbation energies and in all of its components. In contrast, the GPX701 features significantly lower power flux values which cover a larger region, and no distinguishable

tip vortex. There is an area of low perturbation kinetic power flux in the middle of the tip vortex of the GPS609, where *upstream* perturbation kinetic energy has been converted into entropy lost work.

The power fluxes for the GPS609 and GPX701 are integrated on planes extending to one radius of the propeller tip plus two blade heights, encompassing one blade passage, multiplied with the number of blades, and normalized with  $P_{shaft}$ . The resulting values are plotted in Fig. 9. This figure illustrates the main energy conversion process found downstream of a propeller, as manifested by Eq. (11). The main energy conversion occurs between pressure and axial kinetic energy, as the pressure generated behind the propeller disk accelerates the flow. This behavior is also captured in simpler propeller performance models such as the Actuator Disc Model, where pressure is assumed to be increased discontinuously across the propeller disc, and the flow accelerates downstream.

It can also be noted that the kinetic energy of the swirl velocity remains practically constant for the distances shown here, while the energy from the radial component is very small and diminishes downstream of the propeller. For the GPX701 the swirl kinetic energy corresponds to about 16% of the shaft power compared to 11% for the GPS609, which will later in this paper be shown to be due to the peak sectional thrust occurring at lower radii for the GPX701. The entropy lost work is slightly higher for the GPX701 (9.4-10.1%) than for the GPS609 (7.1-8.1%), and the entropy lost work increases continuously with downstream distance due to the mixing of the propeller wakes. It should be noted that most of the work lost to entropy occur when the flow

passes through the blade row, and the downstream increase in entropy (due to mixing) is relatively small in comparison.

The loss terms of Eq. (20) are shown in Fig. 10, and in this figure the velocities have also been decomposed into their circumferential averages and perturbations, thereby allowing an estimation of the tip vortex and wake strengths in terms of shaft power. The main observation here is that the circumferentially averaged velocity components are dominant in the power flows, except for the radial component, which is almost completely a velocity perturbation. The total power of the *perturbation velocities*  $\frac{1}{2}(\Delta v_x^2 + v_{r,2}^2 + v_{\theta,2}^2)$  is found to decay rapidly with increasing distance from the propeller, which is expected due to the mixing occurring downstream of the propeller.

The power flows for the GPX701 have a similar behavior as for the conventional propeller, with the main differences being slightly lower values for the perturbation energies at downstream distances lower than  $0.25D$ , and as mentioned earlier, the higher amount of swirl. The excess axial kinetic energy in the jet  $\frac{1}{2}\Delta U_x^2$  is of similar magnitude in both propellers and increases downstream of the propellers as pressure energy is converted into axial kinetic energy.

The absence of a tip vortex for the GPX701 has been shown in several earlier figures, but is evident also in Fig. 11, where streamlines and the vorticity magnitude have been plotted for the GPS609 and GPX701 at the same downstream distance as Fig. 7 and Fig. 8. The tip vortex is visible through the intertwined streamlines that pass through the tip of the GPS609 and coincide with the high vorticity region on the

downstream plane. This particular type of flow pattern is not discernible in the flowfield of the GPX701.

## 6.2 Performance and flow visualization

The thrust coefficients for the two propellers are presented in Table 2 and the sectional thrust and lift distributions are shown in Fig. 12. Both propellers produce virtually the same thrust, but differ in the radial position where the maximum thrust is generated, which for the GPS609 blade is closer to the tip region, while the GPX701 is higher near mid-span. A similar difference in the location for peak loading can be found for the sectional lift distribution. The radial position of peak sectional thrust/loading is important, since thrust generated near the tip of the blade produces less swirl compared to the same amount of sectional thrust generated near the hub. This is also in line with the wake analysis results shown previously, which showed high amounts of swirl for the GPX701, and explains the difference versus the GPS609.

Mach number contour plots for two radial sections have been selected for illustrating and explaining the differences in the flow field between the analyzed propellers. The chosen radial positions are representative of the different flow fields in the lower and upper blade sections. The flow field around the GPS609 blade, seen in Fig. 13a) and b), behaves as expected, with an extensive region of low pressure on the suction side, and shows no signs of flow separation or strong shocks. The flow field of the GPX701 seen in Fig. 13c) and d), has a more complex structure. In Fig. 13c) a high speed region exists in the blade passage at  $r/R_{tip} = 0.75$  which extends from the

leading blade (LB) suction side to the trailing blade (TB) pressure side. There is also a shock present on the suction side of the leading blade, which extends through the passage but is weaker closer to the pressure side of the trailing blade. The key difference in the flow field between the GPS609 and GPX701 propellers can be seen as the high Mach number region in the GPX701 blade passage. This region decreases the pressure on the pressure side of the trailing blade, leading to lower sectional thrust. This *blade interference* is the most likely cause behind the GPX701 reaching peak sectional thrust at a lower radius, and therefore producing more swirl than the GPS609. Additionally, the round arch shape also decreases the amount of thrust generated above  $r/R_{tip} = 0.85$ .

## 7 DISCUSSION

In comparison to existing propellers the Boxprop is a substantially more recent innovation and there is still a lot to learn about its design principles and potential benefits. Nevertheless, this first attempt to a systematic characterization of the aerodynamic properties of the Boxprop has already shown that it is possible to design it for competitive levels of thrust without producing a tip vortex (see Fig. 7, Fig. 8, and Fig. 11). The levels of thrust obtained by the GPX701 are comparable to the front rotors of published open rotors [25, 26, 27], and the absence of a front rotor tip vortex could mitigate the need for rear rotor clipping in open rotors. This could potentially also increase the efficiency of a counter-rotating open rotor by more effectively cancelling out swirl emanating from the tip region of the front blades, which is impossible when

using a clipped rear blade. This swirl-cancelling effect would be more pronounced at cruise conditions due to the lower slipstream contraction at that operating point. Additionally, the absence of a tip-vortex could have acoustic benefits, especially during take-off conditions, but this would require using transient methods coupled together with an appropriate acoustic analogy, as has been published for a number of open rotor designs [27, 28].

The wake analysis method derived in this paper provides a systematic breakdown of the losses present in propeller flows, and accounts for the main energy transfer process occurring in propeller flows (from pressure to axial kinetic energy, see Fig. 9). Additionally, the velocity decomposition used allows the tip vortices and wakes to be identified clearly and their strength quantified (as is shown in Fig. 8 and Fig. 10) – a unique feature of the theory which the authors have not seen published elsewhere for propellers or open rotors.

The levels of perturbation kinetic energy are similar for both of the analyzed propellers, but a traditional, near-circular tip vortex is not discernible for the GPX701. More specifically, the perturbation kinetic energy of the GPX701 is either concentrated in the wakes of the blade (axial and swirl components) or around the arch-shaped tip (radial component).

The overall levels for entropy lost work  $\phi_s$  as a fraction of shaft power stand at approximately 10% for GPX701 and 8% for the GPS609 (Fig. 9), with peak values occurring at the tip vortex of the GPS609 propeller. The GPX701 flowfield looks fundamentally different, and lacks a similar area of peak entropy lost work, but its

longer span, higher blade area (5%) and stronger shocks result in a slightly higher overall entropy lost work than the GPS609.

The wake analysis method clearly shows that the main area of improvement for the Boxprop design lies in reducing the amount of generated swirl, which according to Fig. 10 accounted for 16% of the shaft power for the GPX701, and 11% for the GPS609. For a Boxprop operating as the front rotor of an open rotor the generated swirl could to a large extent be recuperated by the rear counter-rotating rotor. The amount of swirl is highly dependent on how the blade is loaded with respect to radial position, and as can be seen in Fig. 12, the GPX701 sectional thrust and lift curves peak at lower radii than the GPS609, which leads to more swirl for the GPX701. Examining the Mach number contours (Fig. 13c) of the GPX701 reveals that the blade passage flow at  $r/R = 0.75$  operates at high Mach numbers and therefore low pressure, which decreases the obtainable loading for the trailing blade at this radial position. This blade interference persists all the way to the blade tip, and for equal thrust propellers, forces the GPX701 loading to peak closer to the hub and to generate more swirl than the GPS609.

Although a detailed weight analysis is not carried out within this study it is expected that the higher structural rigidity of the Boxprop blade can be translated into thinner blade sections, especially in the blade root region, which will at least partly compensate for the larger blade retention mechanisms and platforms (compared to a conventional propeller blade).

It is suggested that Boxprop designs reaching the full efficiency potential has to be able to shift loading further out radially to make efficient use of all wetted blade

surface area. Therefore blade interference must be decreased. Several measures could be employed; 1) The trailing and leading blade could be moved upstream and downstream along the flow direction, respectively 2) The leading and trailing blades could be moved away from each other in the propeller tangential direction, in essence making the Boxprop more “bulbous” in shape. Measure 1) and 2) could potentially decrease the blade interference by allowing the suction and pressure sides of each blade half to propagate more freely in space. An illustration of 1) and 2) can be found Fig. 14. 3) Employing custom airfoils could potentially decrease interference. It should be noted that the analyzed propellers are designed with profiles from a standard family and that the position of max thickness and camber have not been varied. It is likely that the interference effects can be reduced by a free optimization of the profile shapes in a similar way that cascades benefit from different profiles than isolated airfoils.

## **8 CONCLUSIONS**

A wake analysis method has been derived which provides a systematic breakdown of the losses present in propeller flows as fractions of shaft power. The method has, in contrast to previous work, removed the assumptions of uniform flow, no radial flow and constant static pressure in the propeller jet. Additionally, it is able to distinguish and quantify the strength of wakes and tip vortices from the mean flow, and provides the means for a direct comparison of different designs. The wake analysis method could potentially also be extended to other types of axial turbomachines.

As has been shown with the wake analysis method, streamlines, and vorticity plots, the Boxprop design presented in this paper (GPX701) features no discernible tip vortex. There is still flow in the radial and swirl directions around the tip of the Boxprop, but it is significantly more spread out than for the conventional propeller. This was also evident in the kinetic energy of the perturbation velocities (wakes and tip vortices), which for the five bladed Boxprop was found to be similar in magnitude to that of the conventional propeller, but the perturbation has lower amplitude, is more spread out, and lacks a near-circular vortex structure.

The blade interference in the GPX701 blade passage limits the thrust that can be generated close to the tip, which for a constant overall blade thrust has to be compensated for by increasing loading closer to the hub. This results in higher amounts of swirl for the present Boxprop design than for the analyzed conventional propeller. Systematic analysis revealed that future designs could possibly alleviate the blade interference by applying forward-sweep on one blade half and back-sweep on the other blade half, thereby increasing the spacing between the two. Alternatively, but riskier in terms of structural mechanics, is to separate the blade halves further in the tangential direction. Lastly, custom airfoil profiles could also possibly reduce the blade interference.

The wake analysis method as presented has provided valuable insight into sources of loss for the Boxprop and will help direct future propeller designs towards improved performance and weaker non-uniformities in the wake.

## **9 ACKNOWLEDGMENT AND FUNDING**

This work was supported by Sweden's Aeronautical research program sponsored jointly by the Swedish Armed Forces, the Swedish Defense Materiel Administration and the Swedish Governmental Agency for Innovation Systems.

## NOMENCLATURE

$A$	Integration area [m <sup>2</sup> ]
$AF$	Activity factor
CROR	Counter-Rotating Open Rotor
$C_P$	Power coefficient
$C_T$	Thrust coefficient
$D$	Propeller diameter, defined from the maximum radius of the stacking line [m]
$D_{hub}$	Propeller hub diameter [m]
$F_x$	Thrust [N]
$F_x'$	Sectional thrust per blade radius [N/m]
$J$	Advance ratio
$L'$	Sectional lift per blade radius [N/m]
$P_{shaft}$	Shaft input power [W]
$R_{hub}$	Propeller hub radius [m]
$R_{tip}$	Propeller tip radius [m]
$T$	Static temperature [K]
$T_\infty$	Static temperature far upstream [K]
$U_i$	Circumferentially averaged velocity component $i$ [m/s]
$\dot{W}$	Work done on the fluid per unit time [W]
$V_\infty$	Velocity far upstream [m/s]
$c$	Airfoil chord [m]

$h$	Static specific enthalpy [J/kg]
$h_0$	Total specific enthalpy [J/kg]
$k$	Turbulent kinetic energy [J/kg]
$\dot{m}$	Mass flow [kg/s]
$n$	Rotational speed [1/s]
$s$	Entropy [J/(kg · K)]
$r$	Radius [m]
$t$	Blade section thickness [m]
$u_i$	Velocity component $i$ [m/s]
$u_n$	Velocity normal to the integration surface [m/s]
$v_i$	Non-axisymmetric velocity perturbation component $i$ [m/s]
$y_{ave}^+$	Average $y^+$ value for the mesh
$\eta_{prop}$	Propeller efficiency
$\zeta$	Energy component [J/kg]
$\rho$	Density [kg/m <sup>3</sup> ]
$\theta$	Azimuth angle
$v$	Specific volume [m <sup>3</sup> /kg]
$\phi_p$	Pressure work
$\phi_s$	Entropy lost work

Subscripts

1	Upstream/inlet plane
---	----------------------

$z$	Plane for wake evaluation
$n$	Normal to integration surface
$r$	Radial component
$\theta$	Swirl component
$x$	Axial component

## 10 REFERENCES

---

- [1] Bowles, Mark D. The "Apollo" of Aeronautics: NASA's Aircraft Energy Efficiency Program, 1973-1987. 2010.
- [2] Hager, Roy D., and Deborah Vrabel, 1988, "Advanced Turboprop Project", NASA Lewis Research Center, Paper No. NASA SP-495.
- [3] Bittar, B. et al, 2011, "PROJECT SAGE2: Enabling Open Rotor Technologies", XX International Symposium on Air Breathing Engines 2011, Gothenburg, Sweden, Paper No. ISABE 2011-1304.
- [4] Clean Sky. "Open Rotor - Safran". Published 2017-06-22. YouTube video, 01:24. Accessed 2017-07-19. <https://www.youtube.com/watch?v=1Bs4ioNbrYA>].
- [5] Prandtl, Ludwig, 1924, "Induced Drag of Multiplanes", NACA, Paper No. NACA TN-182.
- [6] Avellán, Richard, and Anders Lundbladh. "Air Propeller Arrangement and Aircraft", International Patent Application WO2011/081577A1, filed on December 28, 2009.
- [7] Avellán, Richard, and Anders Lundbladh. "Air Propeller Arrangement and Aircraft", U.S. Patent Application 13/519,588, filed December 28, 2009.
- [8] Image credit: "Joined wing" by Steelpillow, licensed under CC BY-SA 3.0. <https://creativecommons.org/licenses/by-sa/3.0/deed.en> Retrieved at 2017-11-30 at [https://upload.wikimedia.org/wikipedia/commons/a/aa/Joined\\_wing.svg](https://upload.wikimedia.org/wikipedia/commons/a/aa/Joined_wing.svg)
- [9] Kroo, Ilan. "Nonplanar wing concepts for increased aircraft efficiency." VKI lecture series on innovative configurations and advanced concepts for future civil aircraft (2005): 6-10.
- [10] AIAA, "NASA Environmentally Responsible Aviation – Lockheed Martin ERA Team" [https://www.aiaa.org/uploadedFiles/About-AIAA/Press-Room/Key\\_Speeches-Reports-and-Presentations/2012/Martin-Lockheed-AVC-AIAA-GEPC2.pdf](https://www.aiaa.org/uploadedFiles/About-AIAA/Press-Room/Key_Speeches-Reports-and-Presentations/2012/Martin-Lockheed-AVC-AIAA-GEPC2.pdf) Retrieved at 2017-11-30.
- [11] Avellán, Richard, and Anders Lundbladh. "Boxprop, a Forward-Swept Joined-Blade Propeller." In ISABE-2013-1108. 2013.
- [12] Avellán, Richard, Alexandre Capitaio Patrao, Anders Lundbladh, and Tomas Grönstedt. "Preparing for Proof-of-concept of a Novel Propeller for Open Rotor Engines." In ISABE-2015-20097. 2015.
- [13] Hall, Cesare, Alexios Zachariadis, Tobias Brandvik, and Nishad Sohoni. "How to Improve Open Rotor Aerodynamics at Cruise and Take-Off." The Aeronautical Journal 118, no. 1208 (2014): 1103-1123.
- [14] Drela, Mark. "Power balance in aerodynamic flows." AIAA journal 47, no. 7 (2009): 1761.
- [15] Denton, J. Do, and N. A. Cumpsty. "Loss Mechanisms in Turbomachines." Journal of Turbomachinery. Transactions of the ASME 115, no. 4 (1993): 621-656.
- [16] Dixon, S. Larry, and Cesare Hall. Fluid Mechanics and Thermodynamics of Turbomachinery. Butterworth-Heinemann, 2013.
- [17] Miller, R. J., and J. D. Denton. "Loss Mechanisms in Turbomachines." Cambridge Turbomachinery Course 2012 1 (2012): 119-179.
- [18] Kotas, Tadeusz Jozef. The Exergy Method of Thermal Plant Analysis. Elsevier, 2013.

- [19] Violette, John A., William E. Sullivan, and Jay E. Turnberg, J.E., 1984, "Large-Scale Advanced Prop-Fan (LAP) Blade Design", Hamilton Standard, Windsor Locks, CT, United States, Paper No. NASA-CR-174790.
- [20] Saravanamuttoo, Herbert Ian Howard, Gordon Frederick Crichton Rogers, and Henry Cohen. *Gas Turbine Theory*. Pearson Education, 2001.
- [21] Drela, M. "Qprop-Theory Document." [web.mit.edu/drela/Public/Qprop](http://web.mit.edu/drela/Public/Qprop) (2006).
- [22] ANSYS Inc, 2012, ANSYS CFX Reference Guide, Version 14.5, Canonsburg, PA, USA.
- [23] ANSYS Inc, 2012, ANSYS CFX-Solver Modelling Guide, Version 14.5, Canonsburg, PA, USA, pp 85.
- [24] ANSYS Inc, 2012, ANSYS CFX-Solver Modelling Guide, Version 14.5, Canonsburg, PA, USA, pp 165.
- [25] Negulescu, Camil A. "Airbus AI-PX7 CROR Design Features and Aerodynamics." *SAE International Journal of Aerospace* 6, no. 2013-01-2245 (2013): 626-642.
- [26] Stuermer, Arne. "Unsteady CFD Simulations of Contra-Rotating Propeller Propulsion Systems." Paper No. AIAA-2008-5218 (2008).
- [27] Stuermer, Arne, and Jianping Yin. "Low-Speed Aerodynamics and Aeroacoustics of CROR Propulsion Systems." *AIAA Paper* 3134 (2009).
- [28] Olausson, Martin, Richard Avellán, Niklas Sörman, Filip Rudebeck, and Lars-Erik Eriksson. "Aeroacoustics and Performance Modeling of a Counter-Rotating Propfan." In *ASME Turbo Expo 2010: Power for Land, Sea, and Air*, pp. 747-756. American Society of Mechanical Engineers, 2010.

### Figure Captions List

- Fig. 2 Illustration of work per unit time added to a fluid element flowing from a point far upstream (1) to a point downstream of the propeller (2). Slice of the area of integration for one blade passage is marked blue behind the propeller blade.
- Fig. 3 GPS609 with direction of airflow and rotation
- Fig. 4 GPX701 with direction of airflow and rotation. Leading (LB) and trailing blades (TB) relative to the direction of rotation are marked.
- Fig. 5 Domain topology. Flow travels from left to right. There is an inner (white) rotating domain containing the propeller blade, and a 2D outer stationary domain (grey). The inlet is marked green, the outlet blue, and the opening boundary is colored yellow. One plane (red) used for the wake analysis is shown behind the propeller.
- Fig. 6 Coarse mesh at the hub region. Flow goes from left to right and the wake block is marked with a blue box. The coarse mesh was

used to evaluate grid convergence, and was refined to provide the data presented.

Fig. 7 GPS609 (upper four plots) and GPX701 (lower four plots) power fluxes ( $W/m^2$ ) for the loss terms in Eq. (14) for a plane located  $0.2D$  downstream of the propeller trailing edge at 75% radius. The axial direction is normal to the page. The values are displayed as multiples of  $10^5$  ( $W/m^2$ ). The axial direction is normal to the page and parallel with the direction of propeller rotation.

Fig. 8 GPS609 (upper four plots) and GPX701 (lower four plots) power fluxes ( $W/m^2$ ) for the kinetic energy terms representing the velocity perturbations, see Eq (20). The contours are shown on a plane located  $0.2D$  downstream of the propeller trailing edge at 75% radius. The values are displayed as multiples of  $10^5$  ( $W/m^2$ ). The axial direction is normal to the page and parallel with the direction of rotation.

Fig. 9 Power integrals  $\int \rho u_n \zeta dA$  for the terms in Eq. (11) - normalized by shaft power as a function of axial distance from the GPS609 (left) and GPX701 (right).

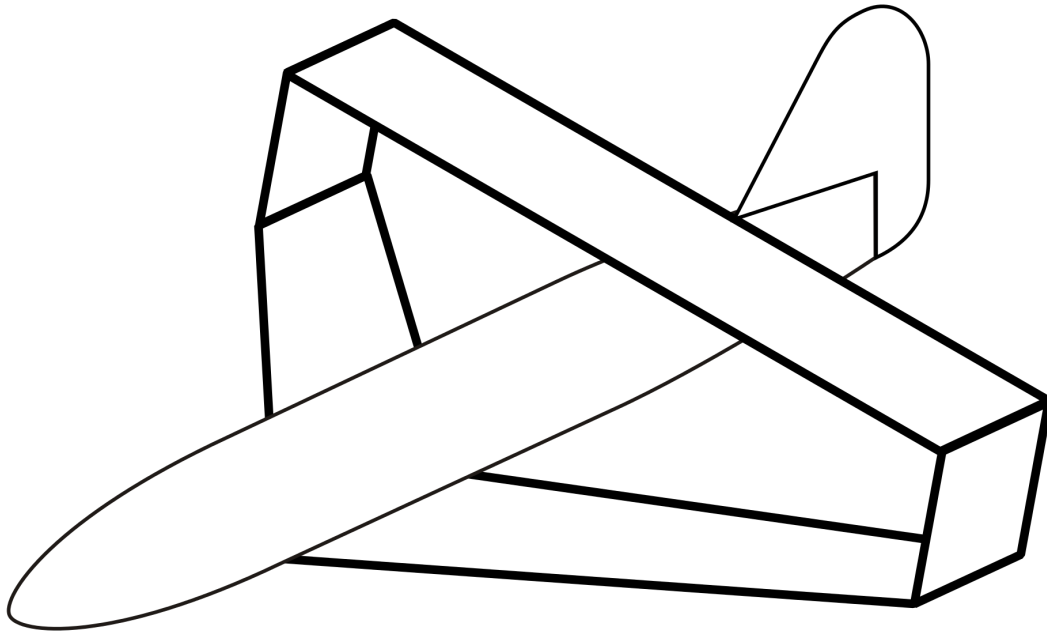
- Fig. 10 Power integrals  $\int \rho u_n \zeta dA$  for the loss terms of Eq. (20) - normalized by shaft power as a function of axial distance from the GPS609 (left) and GPX701 (right). Note the double scale: to the left for entropy lost work and mean velocity energies, and to the right for the perturbation energies.
- Fig. 11 Streamline plots of the flow around the blade tips for the GPS609 (above) and the GPX701 propellers (below). The planes display the vorticity  $0.2D$  downstream of the propeller blade trailing edge, and use identical color scaling.
- Fig. 12 Sectional thrust  $F_x'$  [N/m] for the GPS609 and GPX701
- Fig. 13 Mach number distribution for a) GPS609 at  $r/R_{tip} = 0.75$ , b) GPS609 at  $r/R_{tip} = 0.5$ , c) GPX701 at  $r/R_{tip} = 0.75$  and d) GPX701 at  $r/R_{tip} = 0.5$ . Solid lines denotes Mach 1.
- Fig. 14 Potential design strategies that could be employed to decrease flow interference for the Boxprop. Arrows denote the direction that blade halves can be moved. 1) Involves shearing apart the blade halves along the flow direction, the TB upstream and LB

downstream. 2) Moving the blade halves apart in the tangential direction.

**Table Caption List**

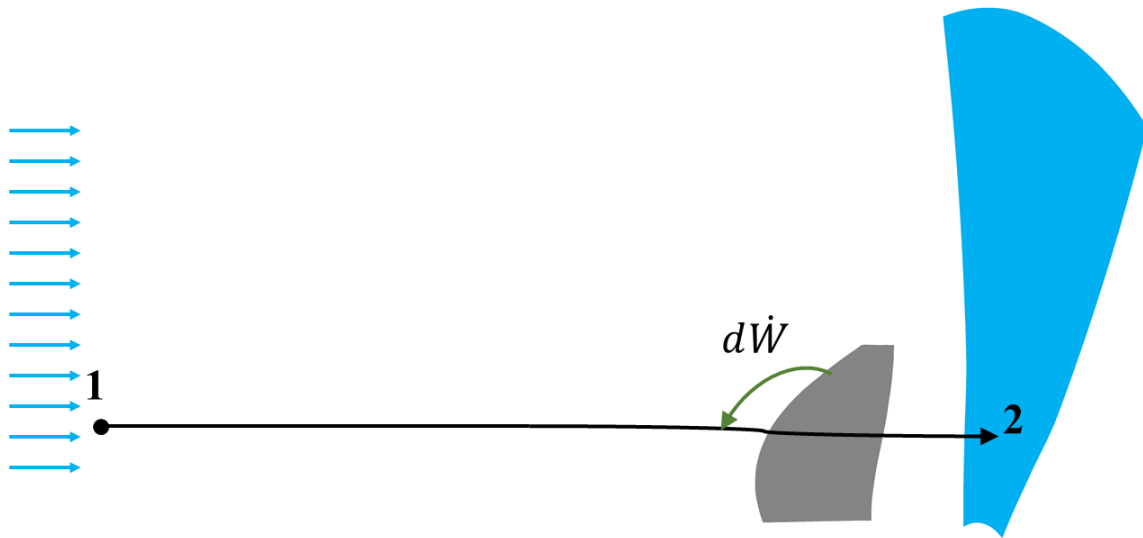
Table 1 Propeller specifications

Table 2 Thrust coefficients for operating point given in section 4



*Fig. 1 – A conceptual sketch of an aircraft incorporating a box wing. Image credit: [8].*

1 COLUMN WIDTH



*Fig. 2 - Illustration of work per unit time added to a fluid element flowing from a point far upstream (1) to a point downstream of the propeller (2). Slice of the area of integration for one blade passage is marked blue behind the propeller blade.*

1 COLUMN WIDTH

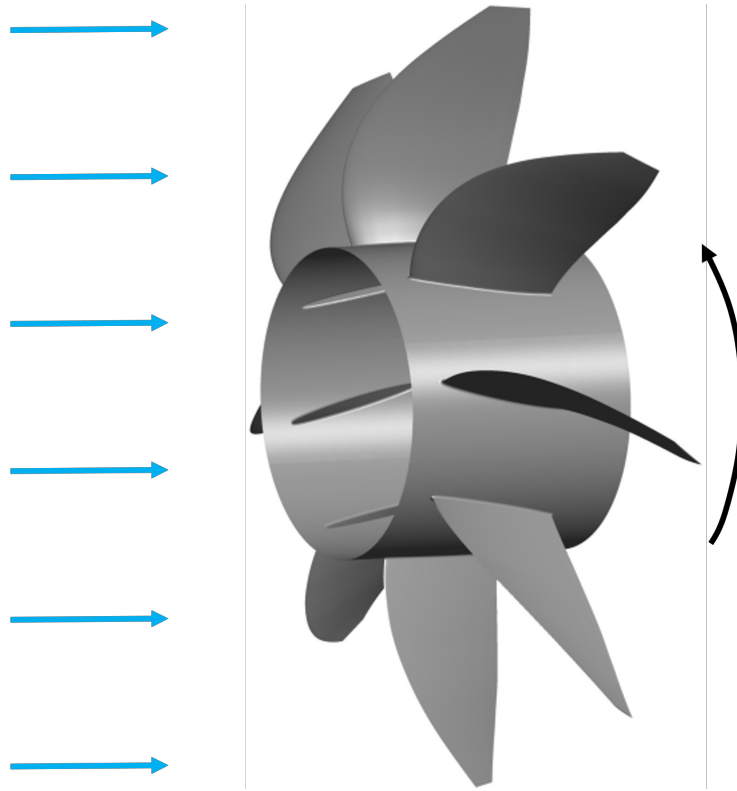


*Fig. 3 - GPS609 with direction of airflow and rotation*

1 COLUMN WIDTH

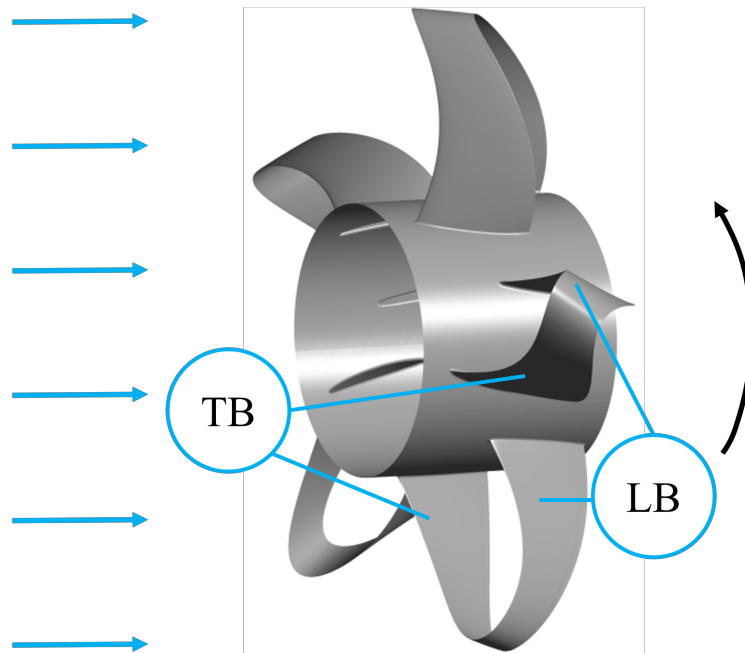


*Fig. 4 - GPX701 with direction of airflow and rotation. Leading (LB) and trailing blades (TB) relative to the direction of rotation are marked.*

1 COLUMN WIDTH

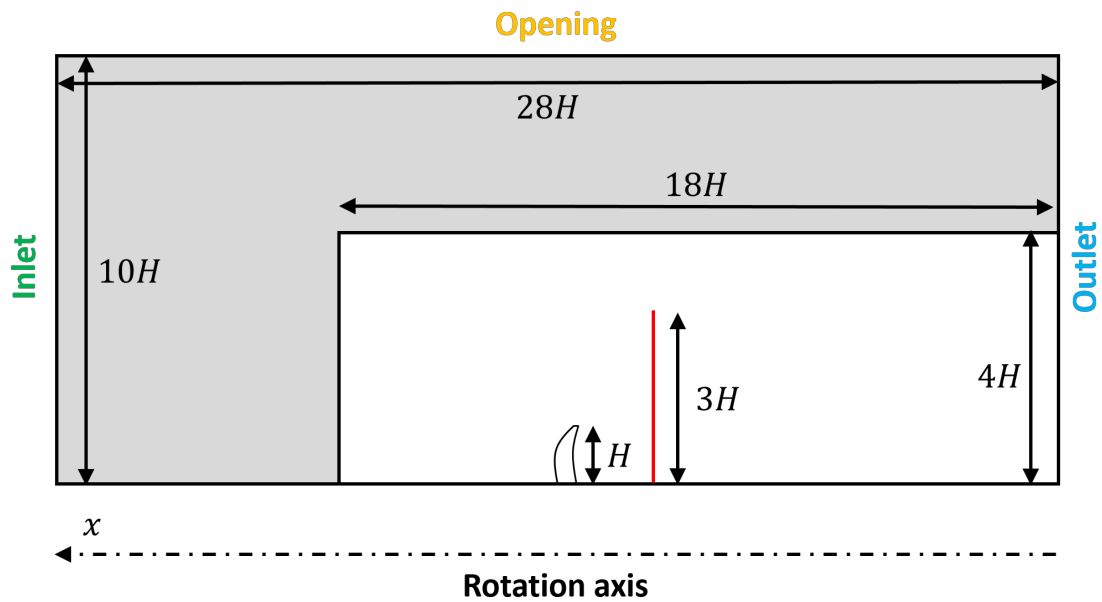
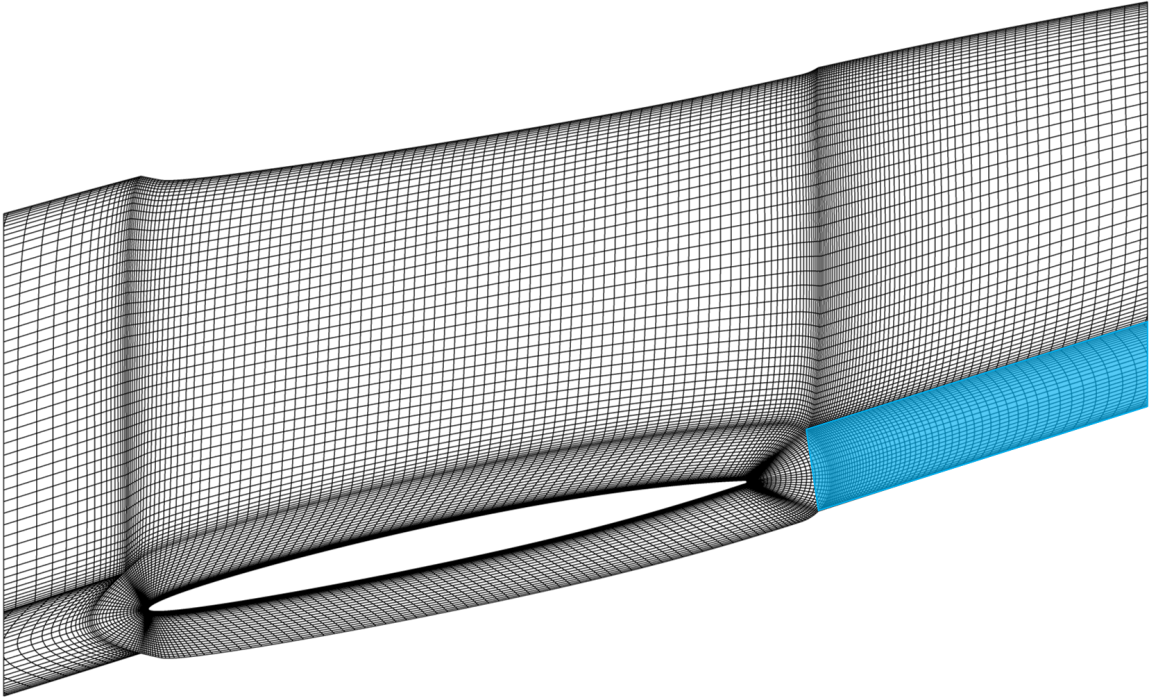


Fig. 5 - Domain topology. Flow travels from left to right. There is an inner (white) rotating domain containing the propeller blade, and a 2D outer stationary domain (grey). The inlet is marked green, the outlet blue, and the opening boundary is colored yellow. One plane (red) used for the wake analysis is shown behind the propeller.

1 COLUMN WIDTH



*Fig. 6 - Coarse mesh at the hub region. Flow goes from left to right and the wake block is marked with a blue box. The coarse mesh was used to evaluate grid convergence, and was refined to provide the data presented.*

1 COLUMN WIDTH

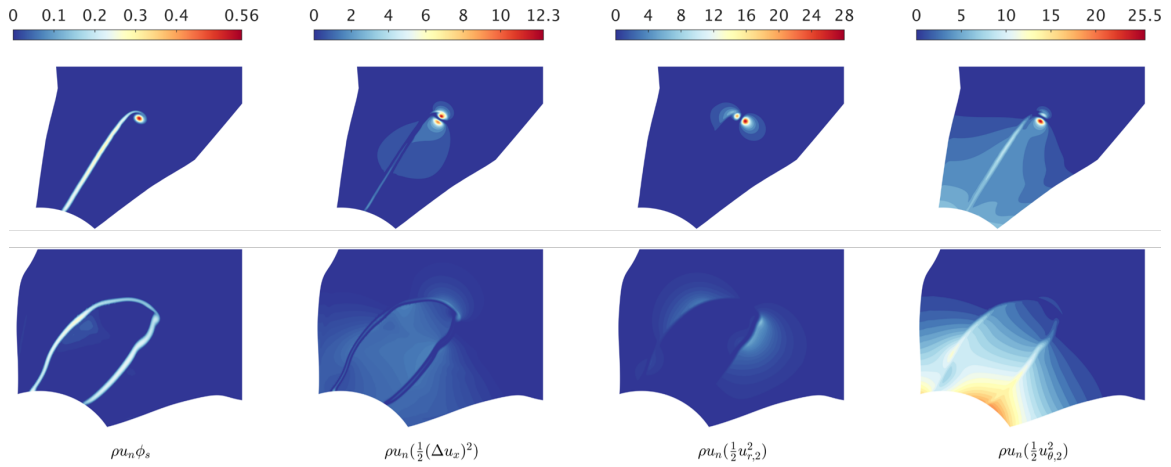


Fig. 7 - GPS609 (upper four plots) and GPX701 (lower four plots) power fluxes ( $W/m^2$ ) for the loss terms in Eq. (14) for a plane located  $0.2D$  downstream of the propeller trailing edge at  $75\%$  radius. The axial direction is normal to the page. The values are displayed as multiples of  $10^5$  ( $W/m^2$ ). The axial direction is normal to the page and parallel with the direction of propeller rotation.

2 COLUMNS WIDTH

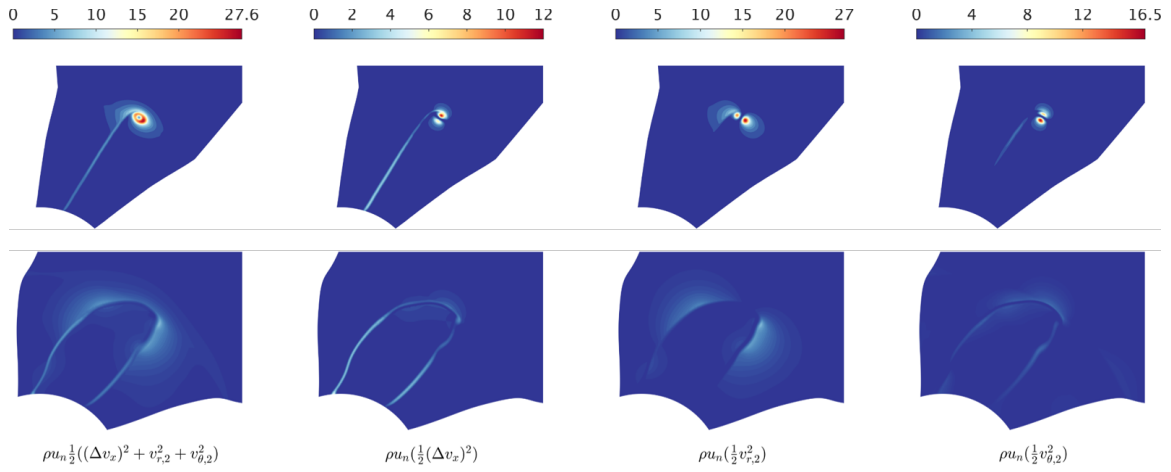


Fig. 8 - GPS609 (upper four plots) and GPX701 (lower four plots) power fluxes ( $W/m^2$ ) for the kinetic energy terms representing the velocity perturbations, see Eq (20). The contours are shown on a plane located  $0.2D$  downstream of the propeller trailing edge at 75% radius. The values are displayed as multiples of  $10^5$  ( $W/m^2$ ). The axial direction is normal to the page and parallel with the direction of rotation.

2 COLUMNS WIDTH

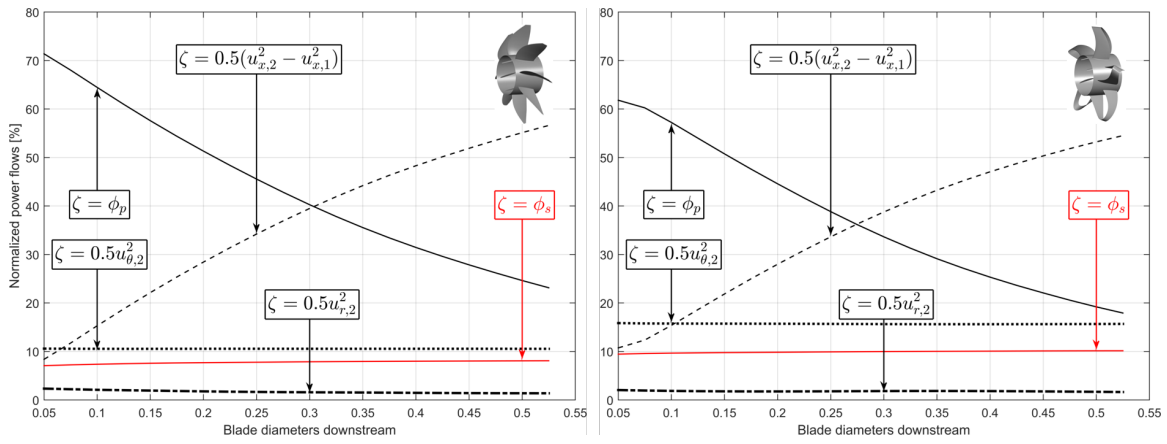


Fig. 9 - Power integrals  $\int \rho u_n \zeta dA$  for the terms in Eq. (11) - normalized by shaft power as a function of axial distance from the GPS609 (left) and GPX701 (right).

2 COLUMNS WIDTH

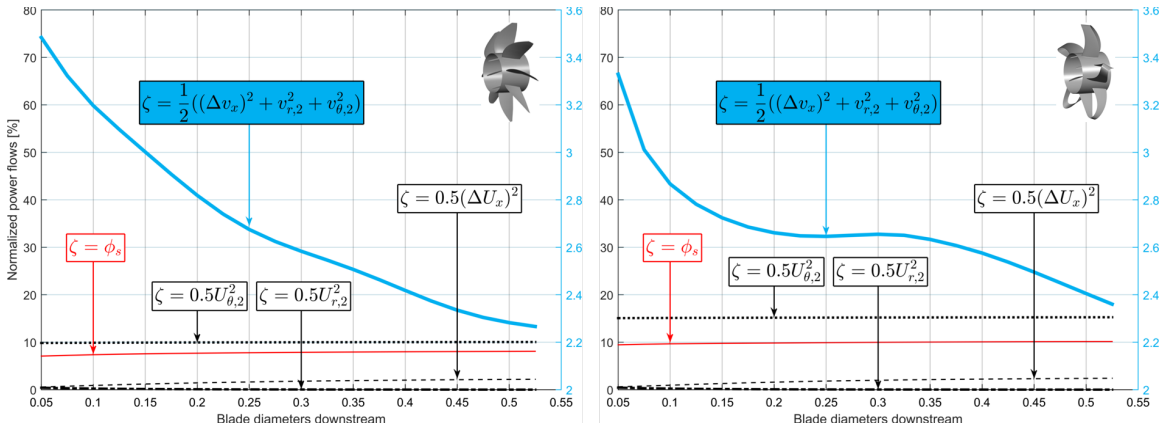
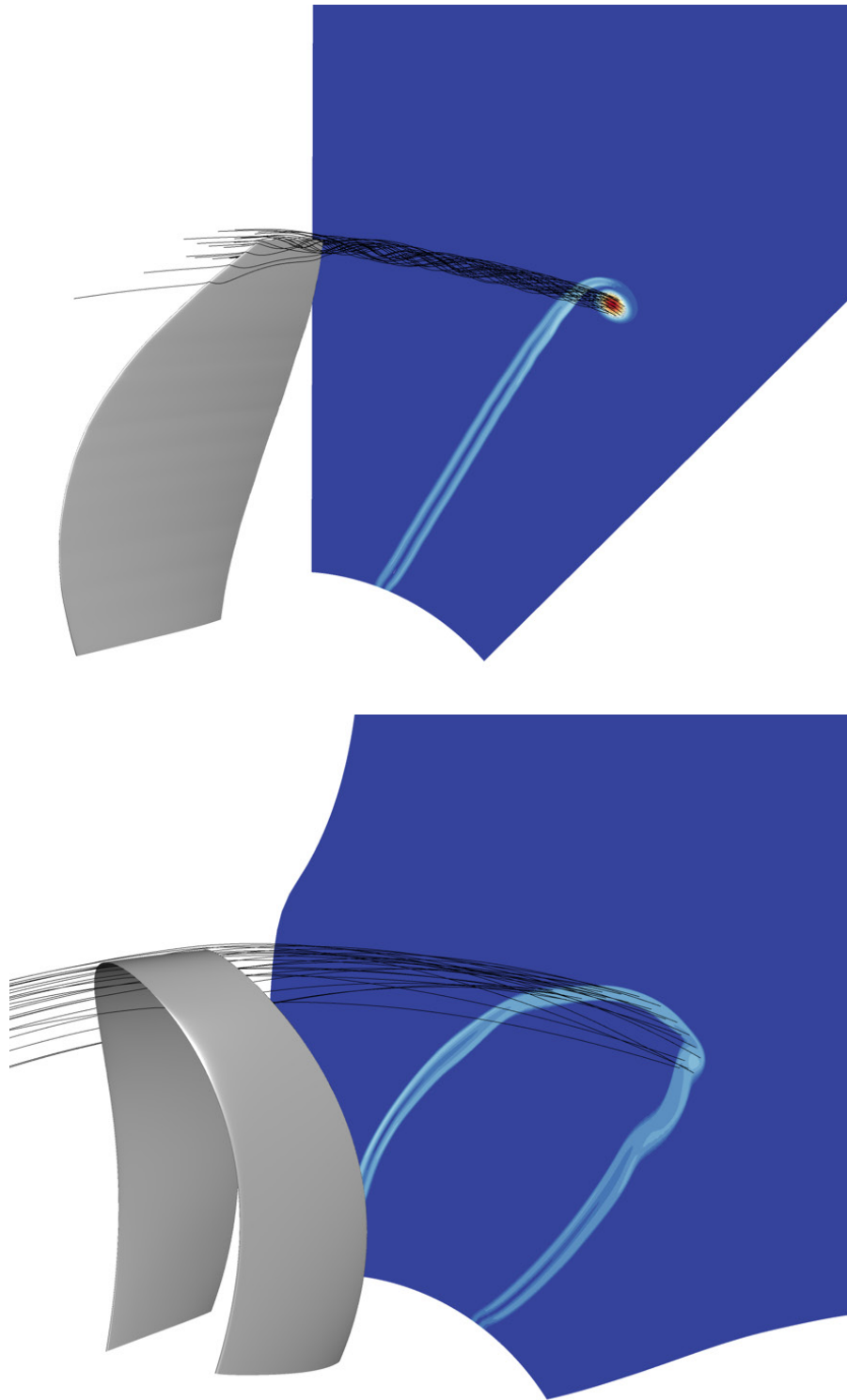


Fig. 10 - Power integrals  $\int \rho u_n \zeta dA$  for the loss terms of Eq. (20) - normalized by shaft power as a function of axial distance from the GPS609 (left) and GPX701 (right). Note the double scale: to the left for entropy lost work and mean velocity energies, and to the right for the perturbation energies.

2 COLUMNS WIDTH



*Fig. 11 - Streamline plots of the flow around the blade tips for the GPS609 (above) and the GPX701 propellers (below). The planes display the vorticity  $0.2D$  downstream of the propeller blade trailing edge, and use identical color scaling.*

1 COLUMN WIDTH

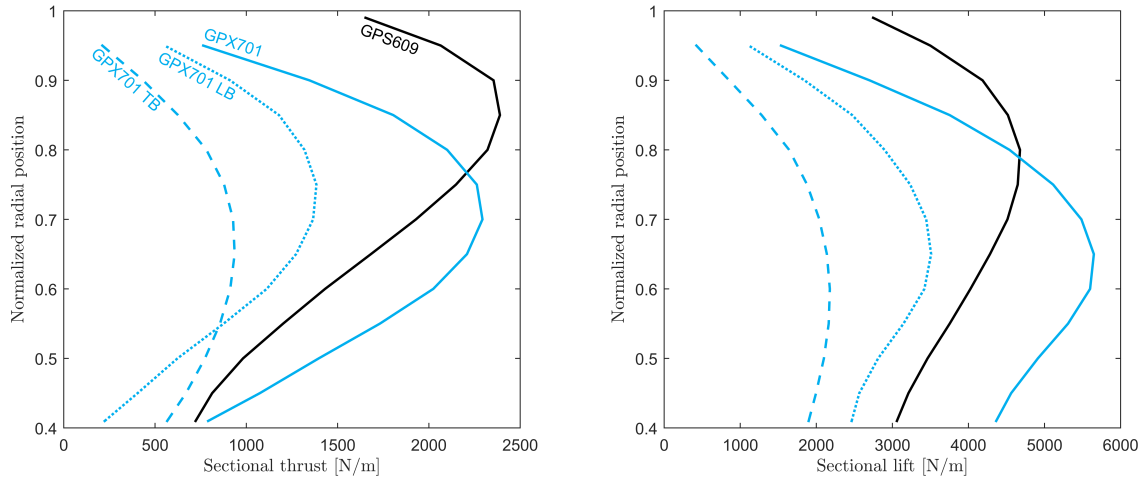


Fig. 12 – Whole propeller sectional thrust  $F_x'$  [N/m] (left) and sectional lift  $L'$  [N/m] (right) for the GPS609 and GPX701

2 COLUMNS WIDTH

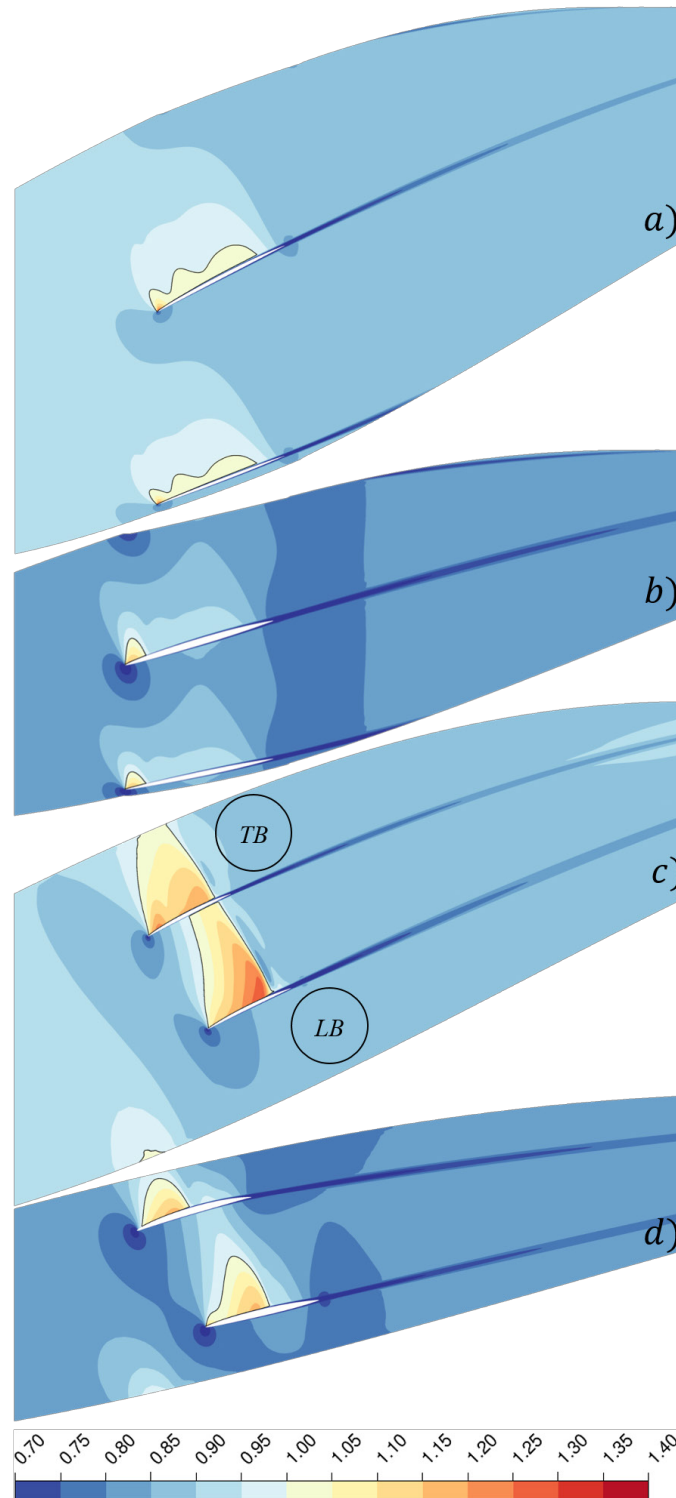
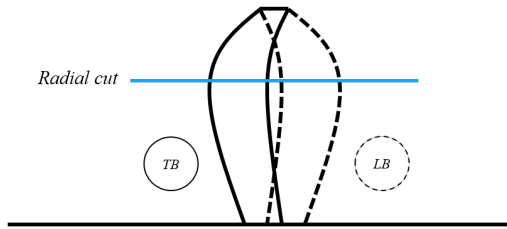


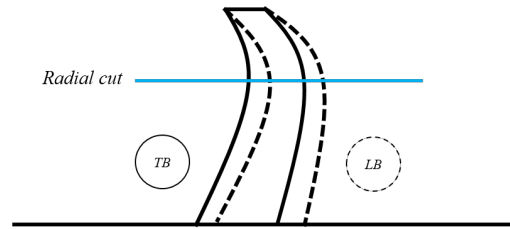
Fig. 13 - Mach number distribution for a) GPS609 at  $r/R_{tip} = 0.75$ , b) GPS609 at  $r/R_{tip} = 0.5$ , c) GPX701 at  $r/R_{tip} = 0.75$  and d) GPX701 at  $r/R_{tip} = 0.5$ . Solid lines denotes Mach 1.

1 COLUMN WIDTH

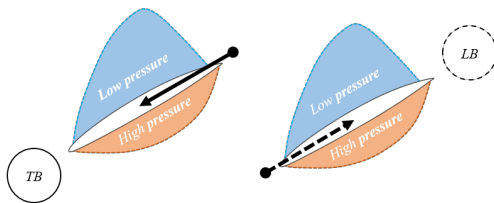
1) Planform



2) Planform



1) Radial cut



2) Radial cut

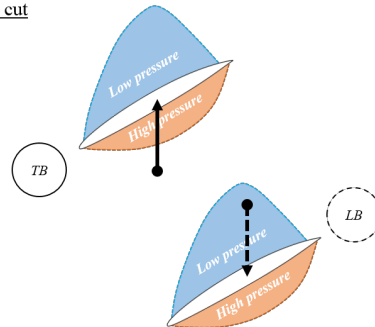


Fig. 14 –Potential design strategies that could be employed to decrease flow interference for the Boxprop. Arrows denote the direction that blade halves can be moved. 1) Involves shearing apart the blade halves along the flow direction, the TB upstream and LB downstream. 2) Moving the blade halves apart in the tangential direction.

2 COLUMN WIDTH

Table 1 - Propeller specifications

	<b>GPS609</b>	<b>GPX701</b>
$J$	3.56	3.56
$n$ [1/s]		83.3
$D$ [m]	0.750	0.750
$D_{hub}$ [m]		0.300
$AF$		1784
<i>Airfoil</i>	NACA 16 series	
$c/D$ [%] <i>Root:</i>	19.4	17.5
$c/D$ [%] <i>Tip:</i>	5.20	9.90
$t/c$ [%] <i>Root:</i>	6.17	6.22
$t/c$ [%] <i>Tip:</i>	2.19	1.64

*Table 2 - Thrust coefficients for operating point given in section 4*

	<b>GPS609</b>	<b>GPX701</b>
$C_T$	0.462	0.463